

This item is the archived peer-reviewed author-version of:

Effect of structural defects on the hydriding kinetics of nanocrystalline Pd thin films

Reference:

Delmelle Renaud, Amin-Ahmadi Behnam, Sinnaeve Marc, Idrissi Hosni, Pardoen Thomas, Schryvers Dominique, Proost Joris.- Effect of structural defects on the hydriding kinetics of nanocrystalline Pd thin films
International journal of hydrogen energy - ISSN 0360-3199 - 40:23(2015), p. 7335-7347
DOI: <http://dx.doi.org/doi:10.1016/j.ijhydene.2015.04.017>
Handle: <http://hdl.handle.net/10067/1264290151162165141>

Effect of structural defects on the hydriding kinetics of nanocrystalline Pd thin films

Renaud Delmelle^{1,*}, Behnam Amin-Ahmadi², Marc Sinnaeve³, Hosni Idrissi^{2,3}, Thomas Pardoën³, Dominique Schryvers² and Joris Proost³

¹ *Laboratory for Hydrogen and Energy, Swiss Federal Laboratories for Materials Science and Technology, Überlandstrasse 129, CH-8600 Dübendorf, Switzerland*

² *Electron Microscopy for Materials Science, Department of Physics, University of Antwerp, Groenenborgerlaan 171, B-2020 Antwerp, Belgium*

³ *Institute of Mechanics, Materials and Civil Engineering, Université catholique de Louvain, Place Sainte-Barbe 2, B-1348 Louvain-la-Neuve, Belgium*

Abstract

While the microstructure of a metal is well-known to affect its equilibrium hydrogen uptake and therefore the hydriding thermodynamics, microstructural effects on the hydriding kinetics are much less documented. Moreover, for thin film systems, such microstructural effects are difficult to separate from the internal stress effect, since most defects generate internal stresses. Such a decoupling has been achieved in this paper for nanocrystalline Pd thin film model systems through the use of a high-resolution, in-situ curvature measurement set-up during Pd deposition, annealing and hydriding. This set-up allowed producing Pd thin films with similar internal stress levels but significantly different microstructures. This was evidenced from detailed defect statistics obtained by transmission electron microscopy, which showed that the densities of grain boundaries, dislocations and twin boundaries have all been lowered by annealing. The same set-up was then used to study the hydriding equilibrium and kinetic behaviour of the resulting films at room temperature. A full quantitative analysis of their hydriding cycles showed that the

* Corresponding author. Phone: +41-58-765.65.41; fax: +41-58-765.69.22; Renaud.Delmelle@empa.ch.

rate constants of both the adsorption- and absorption-limited kinetic regimes were strongly affected by microstructure. Defect engineering was thereby shown to increase the rate constants for hydrogen adsorption and absorption in Pd by a factor 40 and 30, respectively.

Keywords: hydriding; Pd-H; kinetics; adsorption; absorption, microstructure, internal stress

1. Introduction

Microstructure plays a key role in the mechano-chemical properties of materials, including their hydriding properties. In particular, the microstructure of a metal can offer several types of hydrogen trapping sites [1], in the bulk as well as in the surface and subsurface layers. In the case of nanostructured thin films, the contribution of nonbulk-like effects to the total hydrogen content becomes significant, which makes thin films attractive to study microstructural aspects of hydriding.

As a matter of fact, crystalline grains in thin films are very small compared to bulk specimens. The high density of grain boundaries as well as the disordered nature of these defects offers a high concentration of low-energy sites for the absorbed hydrogen atoms, then acting as trapping sites for hydrogen [2]. Using nanocrystalline Pd as a model system, Mütschele and Kirchheim described the distribution of these sites as a Gaussian with a width of 15 kJ/mol [3,4]. Only the low-energy sites are occupied at low hydrogen concentrations, thereby increasing the mean hydrogen concentration. But at high hydrogen concentrations, only the regular lattice sites can be additionally filled with hydrogen. The hydride total volume is less than that of a bulk material, and the mean hydrogen concentration is lowered. Therefore, grain boundaries have a narrowing effect on the miscibility gap of metal-hydrogen systems. This particular distribution of trapping sites in the grain boundaries also affects the hydriding kinetics of metals. At very low hydrogen concentrations, the grain boundary diffusion of hydrogen is virtually stopped by the deepest potential wells [5]. At high hydrogen concentrations, the opposed tendency is observed, and the diffusion in the nanocrystalline material is faster than in Pd bulk [6-8].

Dislocations also play an important role in the hydriding of metals, as the hydrostatic stress component of the hydrogen atoms strongly interacts with the local tensile stress fields that the

dislocation produce [1,9]. Dislocations in thin films are generated by the deposition process, but they can also be created by both hydrogen absorption and desorption [1], where they accommodate the lattice mismatch present when the hydride phase nucleates and grows in the solid solution. In particular, edge dislocations interact strongly with hydrogen atoms, with a binding energy of approximately 60 kJ/mol with the dislocation core [9], i.e. again higher than hydrogen in Pd regular lattice sites [10]. The hydrogen enrichment region at the core of an edge dislocation is seen as cylindrical surface of constant hydrostatic stress located below the dislocation glide plane [11-13]. As opposed to edge dislocations, the shear stress components generated by the screw dislocations interacts poorly with the hydrostatic stress component of the interstitial hydrogen atoms [1]. It is also well-known that dislocations act as preferential pathways for hydrogen transport [14,15], thereby also affecting the hydriding kinetics.

Vacancies, which are other potential hydrogen trapping sites [16], can also be expected in high concentrations in our room temperature deposited metal films. Similarly to the hydrogen interaction with the surface, these open volume defects offer low-energy sites, in which the hydrogen atoms form so-called vacancy complexes whose exact composition and stability are still under debate, even for the Pd-H model system [17-19]. The hydriding kinetics of metals is usually reported to be enhanced by the presence of vacancies [20-22]. Precipitates can also act as hydrogen trapping sites [23], but they won't be considered here, because we only have used pure palladium in this work.

The exact role of twins on the hydrogen absorption by metals remains unclear. Several authors claim that twins can act as hydrogen traps [24,25], but all studies do not confirm these observations. The latter works were carried out on steels, while Danaie et al. concluded that twins do not modify the thermodynamic behavior of hydrogen in magnesium [26]. One can thereby expect that twins can act as traps only if the enthalpy of hydriding in regular lattice sites is high enough, which is not the case for all metals. However, Danaie et al. also observed a significant enhancement in the hydriding kinetics of their Mg powders. Twins can then also

be considered a preferential pathways for hydriding. Amin-Ahmadi et al. have indeed recently shown that nanoscale $\Sigma 3$ {111} coherent growth twin boundaries clearly lose their coherency after hydriding in Pd thin films [27], which may suggest a strong interaction with hydrogen similarly to grain boundaries.

The above studies provide clear evidence that microstructure affect the equilibrium hydriding behavior of metallic compounds. On the other hand, although some of these studies point towards an effect of microstructure on the hydriding kinetics of different metals and alloys, systematic, quantitative studies of this effect are missing, to the best of our knowledge. As opposed to our previous study [28], whose objective was to study quantitatively the effect of internal stress on the hydriding properties of Pd thin films at constant microstructure, this paper is dedicated to the quantitative study of the effect of microstructure on their hydriding properties at constant internal stress. The Pd-H system has been chosen here as a model system since it has been intensively studied for many decades, because of its high storage capacity, its high sensitivity and selectivity to H₂ gas and its ability readily to release hydrogen at room temperature [29,30]. Besides its model system status, Pd is currently still being investigated as a good candidate for applications such as hydrogen sensors [31] and gas purification membranes [32], especially in thin-film form. Additionally, pure Pd is often also used as a catalytic coating [33].

In this study, the microstructure of the Pd films has been controlled by annealing in order to eliminate part of the defects massively generated by the room temperature magnetron sputtering deposition. The annealing process has been coupled to a high resolution in-situ curvature measurement system in order to be able to compare the hydriding properties of the annealed films with as-deposited specimens exhibiting the same initial internal stress state, and to correlate the stress evolution with defect recovery. Many authors indeed identified direct rela-

tionships between the stress evolution during annealing and the density of grain boundaries [34,35], point defects [36,37] and dislocations [34,37,38]. The twin concentration can also be expected to be affected by annealing [39,40], but should not give rise to volume changes, and hence to stress changes (although it is expected to affect the hydriding behavior). Our annealing process will firstly be presented in detail, followed by the study of the equilibrium hydriding behavior of the Pd thin films using the same in-situ curvature measurement approach. The hydriding kinetics of the films will then be studied in quantitative detail, including the determination of the rate-limiting steps and the identification of a microstructural effect on both the adsorption and absorption rate constants. Defect statistics obtained by Transmission Electron Microscopy (TEM) will finally be compared with the internal stress data obtained during annealing and hydriding in order to identify the defects responsible for the microstructural effect on the hydriding equilibrium and kinetics.

2. Experimental

For the purpose of this study, the concept of an experimental setup previously developed for high resolution in-situ monitoring of thin film hydride formation at room temperature [41] has been modified in order to adapt it to high temperature measurements. By relying on experimental knowledge and expertise gained earlier, the setup testing and calibration was relatively straightforward, since the only new issues came from the heating elements. This new setup is schematically shown in Fig. 1.

Here, the vacuum chamber is a T-shaped quartz tube connected to a pumping system from Vacotec SA, consisting of a primary, rotary pump and a turbo molecular pump. Base pressures on the order of 10^{-6} mbar can be reached in the tube in about 20 minutes. Ultra-pure Ar/H₂ gas mixtures (Alphagaz grade from Air Liquide, 1% H₂ in this work) can be introduced into the chamber to instantaneously impose a desired total pressure, which is continuously measured by two electronic gauges (Alcatel ACC 2009 and ASD 2001, total measurement pressure range: $5 \cdot 10^{-9}$ - 1100 mbar).

A high resolution curvature measurement setup (kSA Multi-beam Optical Sensor from k-Space Associates) mounted onto the hydriding chamber continuously detects the positions of multiple laser beams reflecting off a cantilevered sample. The curvature of the latter can be derived from the positions of the laser spots [42]:

$$\Delta\kappa = \frac{\cos \alpha}{2L} \frac{\Delta D}{D_0}, \quad (1)$$

In Eq. (1), $\Delta D/D_o$ is the mean differential spacing between the reflected laser spots in the CCD, L is the distance between the sample and the CCD and α is the angle of laser incidence on the sample. As one can see from Fig. 1, the geometrical configuration of the in-situ curvature measurement is the same as for the hydriding setup described in Ref. [41]. Moreover, the optical distance of the laser beams - as well as their angles of incidence and reflection - have also been kept the same, which led to the same value of the calibration factor ($2L/\cos\alpha = 1.336$ m). As compared to other curvature or deflection measurement techniques, which are generally based on the position detection of a single reflecting laser beam, our setup has a significantly improved dynamic curvature resolution on the order of 10 μm , thanks to the noise minimization resulting from the concurrent use of multiple laser beams. Moreover, thanks to the use of a CCD camera, curvature measurements can be performed with a time resolution better than 100 ms. More details about this optical setup can be found elsewhere [43]. The change in internal stress in the Pd layer, which is simply a result of the prohibited volume change during Pd-H interaction in the thin film geometry, can be straightforwardly derived from the measured changes in sample curvature [42]:

$$\Delta\sigma = \frac{1}{6} \frac{E_S}{1-\nu_S} \frac{t_S^2}{t_f} \Delta\kappa, \quad (2)$$

with $M_S = E_S/(1-\nu_S)$ is the biaxial elastic modulus of the substrate, and t_S and t_f the substrate and Pd film thickness, respectively. Finally, the following direct proportionality can be established between the stress change state and the bulk hydrogen content n in the Pd film, as long as the deformation resulting from the hydriding-induced stresses remains elastic (a condition that will be explicitly validated in section 3.2) [44]:

$$\Delta\sigma = \frac{E_f}{3(1-\nu_f)} \left(\frac{\Delta V}{V} \right) = \frac{E_f}{3(1-\nu_f)} \left(\frac{\Delta v}{\Omega_{Pd}} \right) n \equiv Q \cdot n, \quad (3)$$

where E_f and ν_f are, respectively, the Young's modulus and Poisson ratio of the Pd film, and n is the bulk H/Pd atomic ratio. The ratio between $\Delta V/V$ and n is equal to $\Delta v/\Omega_{Pd}$, where Δv is the characteristic volume change per hydrogen atom and Ω_{Pd} is the mean atomic volume of a Pd atom. Eq. (3) then enables a link between the measured hydriding-induced stress changes $\Delta\sigma$ and the bulk H/Pd atomic ratio n , involving a number of mechano-physical constants, which, for convenience, are grouped together into a single proportionality factor Q .

The furnace is from H & C SPRL. As the quartz tube and the pumping system, it has been specifically designed for this setup. It has the shape of an octagonal right prism, and its eight resistances are circularly displayed around the center of its bases, where two circular holes allow introducing the quartz tube. A third circular hole allows the third extremity of the tube to be inserted in the upper part of the ceramic shield of the furnace, so that the laser beams only travel through vacuum and room temperature air. Insulating foam is used to prevent the heat from escaping from the space left by these 3 holes. Moreover, a continuous room temperature air flux is imposed above the quartz tube optical window when the furnace is running. Any convection effect on the optical measure is thereby avoided. Due to this specific furnace geometry, the heat is homogeneous in the middle of the tube - below the kSA MOS system - where the specimen is located during the experiments. Heating is possible up to 1000°C, and specific temperature profiles can be programmed. A thermocouple has been installed in the middle of the tube in order to be able to measure the specimen temperature in real time. Both thin film hydriding and annealing experiments with in-situ curvature measurement can thereby be performed in this setup in the same conditions, namely with one single clamping. The

clamping of the cantilevered samples has been adapted to the high temperature conditions to which it can be exposed by only using quartz elements.

The cantilevered samples used in this study - cut $3 \times 0.5 \text{ cm}^2$ in size from 180 nm thick, oxidized Si wafers - were coated with a 150 nm thick Pd thin film on top of a 10 nm Ti adhesion layer. These metallic layers were generated by DC magnetron sputtering with real-time monitoring of the specimen curvature thanks to the kSA MOS system, as detailed in a previous publication [28]. As the sputtered films have all been deposited at room temperature in this work ($T/T_m = 0.16$, where T_m is the Pd melting point [45]), and according to the well-known Thornton diagram [46], the low surface mobility of the atoms at such a deposition temperature does not allow for grain boundary migration and recrystallisation and then results in the formation of thin columnar grains with a high concentration of crystalline defects. Since the internal stress in the deposits is a function of the argon sputtering pressure p_{Ar} [47], the latter has been adjusted here in order to obtain different internal stresses in the Pd films. The objective was to deposit a batch of specimens with a zero internal stress level, and another batch exhibiting a tensile internal stress level. Then, the specimens with zero internal stress were annealed so that the stress produced - i.e. tensile stress due to the recovery of growth defects [34,38] - corresponds to the tensile internal stress level of the other batch (see Section 3.1). Fig. 2 shows the stress times thickness product as a function of time (before the Pd layer deposit, during the Ti adhesion layer deposit and after the Pd layer deposit) and of Pd thickness (during the Pd layer deposit) of the two batches studied here. In this figure, an initial, baseline curvature measurement has firstly been carried out before the Ti layer deposition. The latter has been carried out at $p_{Ar} = 3 \text{ mTorr}$ for the two wafers presented here. The stress in this Ti film is slightly tensile during the first stages of deposition, and then becomes compressive after the deposit has turned from isolated aggregates to a homogeneous layer [48]. The growth-induced stress in the Pd layer is slightly compressive in the first tens of nanometers, and then

reaches a constant value given by the slope of the stress*thickness vs. thickness curves. Both the sign and magnitude of the latter were indeed previously observed to strongly depend on the value of p_{Ar} used during Pd deposition [28]. The resulting mean internal stress values of the as-deposited Pd films, further denoted as σ_0 , are shown in Fig. 2. The films thicknesses were checked by cross-sectional scanning electron microscopy.

The specimens annealing parameters have been selected on the basis of 4-point probe electrical resistivity measurements performed in the range 20-350°C. Indeed, the changes of microstructure subsequent to the heating of Pd can be interpreted by measuring its resistivity as a function of temperature [49]. These measurements have been carried out with a Linkam LTS 350 heating and freezing stage connected to an Autolab PGSTAT302N operating in constant-current mode (chronopotentiometry). Currents between 1 and 100 mA have been indifferently imposed, without any difference observed in the voltage evolution as a function of temperature. The voltage resolution is equal to 0.3 μ V. Temperature was monitored with a TMS 94 temperature controller, and recorded with the Linksys 32 software. The distance between each contact point on the specimen was set equal to the specimen width, therefore avoiding the use of any correction factor taken into account the rectangular geometry of the specimen and the fact that the ratio between its length and its width is ≥ 4 [50]. In the thermal cycles presented here, the heating rate was 25°C/min, and the temperature was maintained 5 min at 350°C before the cooling phase. Cooling was performed by turning off the heating element and by making cooling water circulate in the structure of the heating stage. Voltage and temperature were measured in-situ throughout the whole temperature cycle. The temperature coefficient of resistance (TCR) of our Pd thin films has also been extracted from these measurements.

Both low magnification TEM and High Resolution TEM (HRTEM) were used to characterize the Pd films using a TECNAI G2 (FEG, 200 kV) microscope. Bright Field (BF) and Dark

Field (DF) TEM techniques were used to obtain quantitative data on the grain size (width and height) and aspect ratio of the grains, Twin Boundary (TB) density and fraction of grains containing TB. Around 100 grains for each film were included in the analysis. In order to ensure no twins were missed in the BF and DF images, the TEM thin foils were tilted up to $\pm 30^\circ$ along two perpendicular directions. Subsequently, BF images were taken after each 1° tilting. HRTEM was used to investigate the microstructure changes at the atomic scale. The dislocation density was measured by counting extra half planes in HRTEM images. For better visualization of extra half planes, a virtual mask is applied on one g vector in the Fast Fourier Transform (FFT) and then an Inverse Fast Fourier Transform (IFFT) was generated revealing the family of planes related to the selected g. This procedure was done for all main spots in the FFT patterns. The HRTEM measurements of the dislocation density included grains with different local orientations and grain size since these parameters can affect the local dislocation density developed within individual nanograins.

Focused Ion Beam (FIB) thinning with the “lift-out” procedure was used for the preparation of both cross-section and plan-view TEM thin foils.

The hydriding experiments presented here have been carried out at room temperature. The quantitative microstructure-affected kinetic analysis performed in this study has been limited to the low p_{H_2} range 1 - 10 mbar. As will be clarified below, this allows avoiding the $\alpha \rightarrow \beta$ hydride phase transition. As explained above, part of the specimens have been previously annealed up to 300°C , with a heating rate of $15^\circ\text{C}/\text{min}$ imposed to the furnace resistances (resulting in an effective heating rate of $8^\circ\text{C}/\text{min}$ inside the quartz tube, which is known to exhibit a high thermal inertia). The specimens were then maintained 20 min at 300°C before going back to room temperature. The tube was under high vacuum during the annealing cycles (on the order of 10^{-6} mbar).

3. Results and discussions

In this section, the annealing cycles undergone by the Pd films have firstly been optimized through 4-point probe electrical resistivity measurements to identify the onset of defect recovery mechanisms responsible for the generation of tensile stress. These results, combined with practical experimental requirements, enabled to define suitable annealing conditions. The annealing and hydriding cycles derived from the in-situ curvature measurement set-up are then presented and interpreted. Next, kinetic rate expressions are applied to analyze in more detail the complete hydriding cycle, and the kinetic model is extended to address the effect of microstructure on the hydriding kinetics. Finally, the latter results are compared with defect statistics obtained by TEM observations.

3.1 In-situ study of annealing

In the context of the 4-point probe electrical resistivity measurements, the TCR of the films was directly deduced from the in-situ voltage and temperature measurements by the following reasoning: as the electrical measurement is performed in constant-current mode, the ratio $\Delta U/U_0$ between the voltage U at a given temperature and the voltage U_0 at room temperature is equal to $\Delta R/R_0$, where R is the specimen electrical resistance. This ratio is itself linked to the TCR by the following relationship [51]:

$$\frac{R}{R_0} = 1 + \alpha(T - T_0), \quad (4)$$

where α is the film TCR, expressed in K^{-1} . At temperatures close to the ambience, this coefficient can be expected to be constant [52], reflecting the classic behaviour of the resistivity of

metals at such temperatures, driven by electron-phonon scattering. But according to Matthiessen's rule, two other sources of electron scattering exist, i.e. defects and impurities. Although our Pd thin films have already been proven to be highly pure [28,41,44], one also knows that the latter contain a lot of crystalline defects. Their contribution to the resistivity of the material is independent of temperature as long as their concentration is not affected by recovery, recrystallisation or grain growth mechanisms. If the temperature is high enough for such mechanisms to occur, defect-free channels are created into the lattice, thereby decreasing the TCR. Fig. 3 shows the evolution of the ratio $\Delta R/R_0$ as a function of temperature during a heating cycle performed on a cantilever covered with a Pd film specimen. The behavior of this ratio during heating up to 200°C shows that the film is responding normally to the electron flow travelling through it, without any apparent change in its concentration of defects. The slope of the curve, i.e. the TCR of the film, starts to decrease between 200 and 210°C, indicating the onset of defect recovery. The temperature plateau at which the Pd films will be maintained during the annealing cycles must thereby be chosen at least above 200°C. The rest of the heating cycle shows that the specimen resistance is slightly increasing during the temperature plateau, probably because the specimen temperature still slightly increases in this time interval. The cooling phase only reflects the temperature dependence of the thermal resistivity of the film, thereby exhibiting the same TCR as before the onset of defect recovery, as expected. The TCR of the films has been estimated in the interval [20-200°C] from specimens with different thicknesses in order to compare it to available literature data. The results - shown in Fig. 4 - indicate that the TCR of our nanocrystalline Pd thin films is smaller than the bulk value ($3.77 \cdot 10^{-3} \text{ K}^{-1}$ [51]), as expected [51,53,54]. One can also clearly see that the TCR increases with increasing film thickness, as previously reported [51,54]. According to Wedler and Alshorachi, the TCR of a thin film can be expressed as a function of its thickness as follows [51]:

$$\alpha = \alpha_0 \left(\frac{1}{1 + K'l_0/t_f} \right), \quad (5)$$

where α_0 is the TCR of the bulk material having the same density of imperfections as the film. l_0 is the mean free path of the electrons and K' is a proportionality factor. A reliable value of l_0 is impossible to obtain, as the electrons in Pd do not behave as a free electron gas. These two last factors thereby cannot be estimated separately. A fit of the TCR with Eq. (5) is performed in Fig. 4, with α_0 and $K'l_0$ as free parameters. Our data appear to be in excellent agreement with those of Wedler and Alshorachi, confirming the trend previously expected by them. More quantitatively, the fit results in $\alpha_0 = 3.1 \pm 0.2 \cdot 10^{-3} \text{ K}^{-1}$, smaller than the bulk value, which indicates that the films contain a high concentration of crystalline defects, as expected.

As shown in Fig. 5, a temperature plateau of 300°C, combined with an annealing time of 20 minutes, and performed on a cantilever from the batch initially exhibiting a growth stress of -35 MPa, gave rise to a final internal stress of 490 MPa, similar to the specimens exhibiting an as-deposited internal stress of 491 MPa. These experimental conditions have therefore been chosen for the kinetic analysis performed in this paper. Note that the internal stress cannot be measured throughout the whole cycle because the laser system has not been designed to work for periods as long as half a day, which is the time necessary for the tube to reach back room temperature from temperature plateaus of several hundreds degrees Celsius. The film internal stress is therefore measured during heating, high temperature maintaining and during the beginning of cooling. When the annealing cycle is over, the stress final value is also measured during 500 sec. During the annealing cycle presented in Fig. 5, the biaxial stress σ undergone by the film can be divided into the following structure-dependent components [34]:

$$\sigma = \sigma_0 + \sigma_{th} + \sigma_i + \sigma_e, \quad (6)$$

where σ_i is the intrinsic stress, consisting, in the case of thin film annealing, in the contribution from a structure evolution mechanism, i.e. volume changes (shrinkage) due to the elimination of growth defects such as grain boundaries, dislocations and point defects [37]. This contribution is tensile, as opposed to hydriding-induced stress. The thermal stress component σ_{th} depends on both thermal expansion coefficients of the film (α_f) and of its substrate (α_s), according to the following law [34,55]:

$$\sigma_{th} = \frac{E_f}{1-\nu_f} (\alpha_s - \alpha_f) (T - T_d), \quad (7)$$

where T is the temperature at which σ_{th} is measured and T_d is the film deposition temperature. In this work, T_d is room temperature, and consequently $T - T_d$ is positive during the entire annealing cycle. Therefore, the thermal stress is expected to be compressive, since $\alpha_s = 0.56 \cdot 10^{-6} \text{ K}^{-1}$ [56] and $\alpha_f = 11.8 \cdot 10^{-6} \text{ K}^{-1}$ [57]. The extrinsic stress σ_i - attributed to structural misfit, phase transformation, precipitation, plastic or creep deformation, chemical reactions, etc. [38] - can be neglected here, taken in to account the yield stress of nanocrystalline Pd in tension [58] and in compression [59].

During the heating phase in Fig. 5, the total stress change ($\sigma - \sigma_0$ in Eq. (6)) is equal to -311 MPa. Knowing that $E_f = 121 \text{ GPa}$ and $\nu_f = 0.39$ [45], and using Eq. (7), one obtains $\sigma_{th} = -602 \text{ MPa}$. This results in $\sigma_i = 291 \text{ MPa}$. This contribution is tensile, as expected. A substantial concentration of growth defects is then recovered in the heating phase, which is logical because the temperature is above the Pd deposition temperature right from the beginning of the experiment. Due to the thermal inertia of the quartz tube, its temperature still slightly increas-

es when the temperature of the furnace resistances is kept constant during the temperature plateau. During this temperature plateau, the stress goes in the tensile direction, as expected because the additional thermal stress is very small. The total stress change is equal to 182 MPa, and the thermal stress is equal to -45 MPa. At 300°C, the amount of defects recovered is important, thus giving rise to an intrinsic stress of 227 MPa. Finally, the total stress change during the cooling phase is equal to 654 MPa, very close to the 647 MPa predicted by Eq. (7). This indicates that the defects recovery process that has been activated through this thermal cycle is almost complete, and that the amount of tensile intrinsic stress produced during the cooling phase is only 7 MPa.

3.2 Hydriding cycle: equilibrium analysis

Fig. 6 shows two hydriding cycles recorded at similar hydrogen partial pressures. One of the Pd films used in these experiments has been directly cut out of the wafer exhibiting 491 MPa internal stress, while the second one comes from the other deposit and has undergone an annealing cycle into the quartz tube - so that these films have very close internal stress levels before hydrogen introduction, as explained above - before being subjected to hydrogen cycling. From Fig. 6, it appears that the as-deposited specimen exhibits a faster hydriding kinetics than the annealed specimen. The time needed for chemical equilibrium to be reached between gaseous hydrogen in the quartz tube and atomic hydrogen inside the Pd film differs of one order of magnitude, the latter raising from about 100 sec for the as-deposited specimen to about 1000 sec for the annealed specimen. This is the expected behaviour for a film containing less growth defects. As discussed above, some of these growth defects - namely, grain boundaries, dislocations, twins and vacancies - have recently been shown to act as pathways for hydrogen transport, thereby potentially accelerating the kinetics of mechanisms such as hydrogen disso-

ciation on the surface, surface-to-bulk transition or diffusion. This issue will be quantitatively considered in next section.

In this study, 5 cantilevers from each wafer considered in Fig. 6 have been hydrided at different p_{H_2} -values. In Fig. 7, the equilibrium absolute stress has been plotted as a function of $(p_{H_2})^{1/2}$ for these 10 experiments. Let us firstly address the assumption of elastic deformation in the Pd films, which is mandatory in order to properly derive their hydrogen content with Eq. (3). As can be seen in Figs. 2 and 5, their tensile as-deposited growth stress is, in the worst case, on the order of 500 MPa, as well as the internal stress reached after annealing. This value is below the nanocrystalline Pd tensile yield stress measured by Colla et al. for Pd thin films with similar thickness and grain size [58]. Furthermore, as the present study has been limited to the low p_{H_2} range 1 - 10 mbar, and as we already showed in previous papers that this range ensures to remain in the α phase of the palladium hydride [28,44], one can expect the absolute internal stress levels at equilibrium to be low enough to avoid plasticity effects accompanying the $\alpha \rightarrow \beta$ phase transition. As can indeed be seen in Fig. 7, the absolute internal stress at equilibrium is far below the 1 GPa compressive yield strength of nanocrystalline palladium measured by Youngdahl et al. [59]. Even at $p_{H_2} = 10$ mbar, the absolute stress does not exceed -350 MPa.

Eq. (3) is thus applicable here, which enables computing the well-known Sieverts' constant ($K_S = (p_{H_2})^{1/2}/n_{eq}$ [29]). The subscript "eq" refers here to the equilibrium H-uptake, so that n_{eq} can be derived directly from Fig. 7 using Eq. (3). By taking $\Delta v / \Omega_{Pd} = 0.19$ [60], $E_f = 121$ GPa and $\nu_f = 0.39$ [45], this results in $K_S = 2.4 \pm 0.5 \text{ atm}^{1/2}$ for the as-deposited batch and $K_S = 2.2 \pm 0.3 \text{ atm}^{1/2}$ for the annealed batch. As expected, these values indicate that the Pd films contain a high concentration of structural defects compared to bulk Pd [61], even after annealing. However, the intercept of the linear fits performed in Fig. 7 shifts by 180 ± 98 MPa in the

compressive direction for the annealed specimen, independent of the hydrogen partial pressure. This would mean that, even if the most defected specimens contain more hydrogen, they involve a sensitivity to p_{H_2} similar to the annealed specimen. Consequently, part of the hydrogen absorbed by the Pd films should be located in saturable trapping sites, which are readily fully filled over the whole p_{H_2} -range considered in this study. Hydrogen trapping sites in metals are indeed commonly divided into unsaturable and saturable sites [62,63], part of the latter being irreversible [64,65], i.e. potential wells being too deep to allow the hydrogen atoms to escape without external energy source. Frappart et al. recently found out that the irreversibly trapped hydrogen concentration is constant in the elastic regime [66], which is consistent with our results. This is not the case for the interstitial hydrogen and the reversibly trapped hydrogen, which are both sensitive to the hydrogen partial pressure. Although potential wells corresponding to the reversible traps are deeper than these of the octahedral interstitial sites of the Pd lattice, reversibly trapped hydrogen is still in equilibrium with interstitial hydrogen. The Sieverts' constant of a material thereby reflects the presence of interstitial hydrogen and reversibly trapped hydrogen. Consequently, our results indicate that the reversible traps are not significantly modified by annealing, while irreversible traps - like dislocation cores [66] - are affected. If the as-deposited specimens contain more irreversible traps than the annealed specimens, this would also mean that the residual compressive stress change observed at the end of the hydriding cycles - reflecting the presence of irreversibly trapped hydrogen, and then independent of p_{H_2} in α -PdH as already inferred in previous studies [28,44] - must be higher when submitting an as-deposited Pd thin film to hydrogen cycling. These values are, respectively, 403 ± 31 MPa for the as-deposited films and 192 ± 14 MPa for the annealed films. A compressive stress difference of 211 ± 34 MPa is then observed, confirming the statement that a higher concentration of irreversible trap sites is present in the as-deposited specimens. Moreover, this value fits well with the 180 ± 98 MPa observed at equilibrium.

3.3 Hydriding kinetics

As kinetic analyses we performed earlier regarding the hydriding of Pd thin films [28,44], the present kinetic analysis has been limited to the low p_{H_2} range 1 - 10 mbar, and our kinetic model - able to provide a self-consistent interpretation of the room temperature hydriding cycle in this range - is an appropriate tool in the context of the present study. One can find a complete description of this kinetic model elsewhere [44]. To summarize, one will start from the observation that two mechanistic steps are potentially rate-limiting, i.e. H_2 adsorption and its dissociative chemisorption on the Pd surface and surface-to-bulk transition:



where s and i are a free surface adsorption site and an interstitial bulk absorption site, respectively, while H-s and H-i represent, respectively, a surface and bulk site occupied by atomic H. As the present hydriding experiments have been performed at room temperature, the diffusion time of the hydrogen atoms in 150 nm thick Pd films - on the order of the millisecond - is too small to be considered as potentially rate-limiting in this kinetic analysis. As to the latter, its constitutive equations have been derived by assuming one of the two mechanistic steps to be rate-limiting, and the other one to be in a pseudo steady-state, as commonly performed in chemical kinetics when dealing with complex second order reactions [67]. The time evolution dn/dt of the bulk H/Pd atomic ratio when the rate-limiting step is, respectively, reaction (8) and (9), have thus been derived in the following forms [44]:

$$\left(\frac{dn}{dt}\right)_{ad} = \frac{2k'_{ad}K_{ab}^2}{(K_{ab} + n)^2 + K_{ab}} [p_{H_2} - (K_s n)^2], \quad (10)$$

$$\left(\frac{dn}{dt}\right)_{ab} = k'_{ab} \left[(1-n) - \frac{K_s n}{\sqrt{p_{H_2}}} \right]. \quad (11)$$

In these equations, $K_{ad} \equiv k'_{ad}/k''_{ad}$ and $K_{ab} \equiv k'_{ab}/k''_{ab}$ are, respectively, the equilibrium constants of reactions (8) and (9).

As systematically observed before [28,41,44], the hydriding cycles performed on the Pd thin films studied here show three characteristic kinetic regimes (see Fig 6). A linear kinetic regime is firstly observed, and has been shown to be limited by absorption. A transition to a second linear kinetic regime - limited by adsorption - is then observed, as a result of a change of the heat of adsorption in the positive direction as the surface coverage reaches a critical value. Later on in the hydriding cycle, the adsorption equilibrium becomes reached, but hydrogen atoms are still absorbed into the bulk. This marks the beginning of a third, nonlinear kinetic regime, limited by absorption. This last regime ends when the absorption equilibrium is finally reached (see Ref. [44] for more details about this kinetic interpretation). The slopes of the first and second kinetic regime have then been plotted as a function of p_{H_2} in Figures 8 and 9, and fitted according to Eq. (11) and (10), respectively. As a previous investigation of k'_{ab} showed that it exhibits a linear dependence with p_{H_2} [28], the latter has also been taken into account in the fits shown in Fig. 8. However, that figure firstly shows that the microstructure of the Pd films has an important effect on their absorption velocity, the annealed specimens being critically slowed down in the first kinetic regime. At least one of the parameters of Eq. (11) must then be affected by microstructure. As K_s has already been shown to be very similar for the two batches, this microstructure-sensitive parameter should be k'_{ab} . Fig. 9 shows the same trend, i.e. an important decrease of the absorption velocity of the annealed Pd thin films in the second, adsorption-limited kinetic regime. As opposed to internal stress,

which has been previously shown to have no effect on the adsorption-related parameters of Eq. (10) [28], microstructure affects both absorption and adsorption-related parameters. As regards these of Eq. (10), K_{ab} should indeed stay the same if the concentration of reversible traps present on the surface and in the bulk is not significantly modified, as discussed in previous section. One may thereby expect k'_{ad} to be affected by microstructure as well.

Let us firstly address the case of the rate constant for hydrogen absorption k'_{ab} in the first kinetic regime. Eq. (11) can be easily integrated, providing a direct access to k'_{ab} [44]. Fig. 10 shows the obtained values of k'_{ab} in the first kinetic regime. A factor 30 is observed between the k'_{ab} values of the annealed specimens and the as-deposited specimens. This factor can be understood by detailing the slopes of the linear fits shown in Fig. 10 as follows [28]:

$$\left\{ \begin{array}{l} \frac{k'_{ab,dep}}{P_{H_2}} = A'_{ab,dep} \exp\left(\frac{-\Delta H_{ab,dep}^{0\ddagger}}{RT}\right) \\ \frac{k'_{ab,an}}{P_{H_2}} = A'_{ab,an} \exp\left(\frac{-\Delta H_{ab,an}^{0\ddagger}}{RT}\right) \end{array} \right., \quad (12)$$

where the subscripts “dep” and “an” are indicative for the as-deposited batch and the annealed batch, respectively. The data from Fig. 10 gives $k'_{ab,dep}/k'_{ab,an} = 30.2 \pm 4.3$. Two possibilities can be considered here to explain this proportionality, i.e. an effect of microstructure on the pre-exponential factor A'_{ab} and an effect of microstructure on the activation enthalpy change for hydrogen absorption $\Delta H_{ab}^{0\ddagger}$. The first possibility results in $A'_{ab,dep}/A'_{ab,an} \cong 30$. In their hydrogen membrane permeation model [68], Ward et al. stated that the jump attempt frequency for bulk-to-surface transition can be considered as very similar to that for diffusion in Pd because the H atom is jumping from a bulk interstitial site in both cases, and that the pre-exponential factor for hydrogen surface-to-bulk transition (A'_{ab} here) is then directly propor-

tional to the jump attempt frequency for hydrogen diffusion. Recent extensive studies of the effect of hydrogen trapping on the diffusion mechanism already showed that the jump attempt frequency for hydrogen diffusion is lowered by the trapping phenomenon because part of the hydrogen atoms are located in potential wells that are deeper than the regular lattice sites [63,64,69]. This undoubtedly rules out the hypothesis that $\Delta H_{ab,dep}^{0\ddagger} = \Delta H_{ab,an}^{0\ddagger}$ in this study. If one considers now the second possibility, i.e. that $\Delta H_{ab}^{0\ddagger}$ is the main microstructure-affected parameter, then one can express the activation enthalpy changes for hydrogen absorption as follows:

$$\begin{cases} \Delta H_{ab,dep}^{0\ddagger} = E_a \\ \Delta H_{ab,dep}^{0\ddagger} = E_a + E_d \end{cases}, \quad (13)$$

where E_a is the activation energy needed for a hydrogen surface-to-bulk transition in the as deposited film and E_d is the energy change due to the recovery of growth defects, one would get $E_d \cong \ln 30 \cdot RT = 8.5$ kJ/mol by combining Eqs. (12) and (13). This means that part of the surface defects are eliminated by annealing as well, resulting in an increase of the activation energy for surface-to-bulk transition, thereby slowing down the absorption kinetics (this situation is schematically illustrated in Fig. 11). This conclusion is realistic, as the energy of structural defects in palladium does not exceed 60 kJ/mol [70], while the energy of regular surface sites is higher, on the order of 100 kJ/mol [33,71]. Moreover, as discussed above, one may expect $A'_{ab,dep} < A'_{ab,an}$. Consequently, we have shown here that reduction of the activation energy for surface-to-bulk transition in nanocrystalline Pd by defect introduction can be on the order of 10%. This result may lead to interesting engineering applications in hydrogen storage materials, hydrogen separation membranes or hydrogen detection.

As already shown in previous studies [28,44], Eq. (10) can be solved by using a 4th order Runge-Kutta algorithm to simulate the temporal evolution of n in the second, adsorption-limited kinetic regime. Fitted values of k'_{ad} have been extracted from this simulation for the two batches considered here. As expected from the trends showed in Fig. 9, k'_{ad} is higher for the as deposited batch ($(2.6 \pm 0.5) \cdot 10^{18} \text{ mbar}^{-1} \text{ s}^{-1}$) than for the annealed batch ($(7 \pm 2) \cdot 10^{16} \text{ mbar}^{-1} \text{ s}^{-1}$). The jump attempt frequency for hydrogen adsorption seems to be increased by the presence of additional surface sites generated by the surface defects induced by thin film growth. As also inferred before [28,44], no trend as a function of p_{H_2} is visible in the k'_{ad} data.

Finally, the rate constant for hydrogen absorption has been calculated in the third kinetic regime, also with Eq. (11). As expected from previous calculations performed in that kinetic regime [28,44], no trend is again visible as a function of p_{H_2} in the k'_{ab} data. The as-deposited batch provides $k'_{ab} = (4.2 \pm 1.7) \cdot 10^{-3} \text{ s}^{-1}$ and the annealed batches provides $k'_{ab} = (2.5 \pm 0.7) \cdot 10^{-4} \text{ s}^{-1}$. This confirms the trend discussed above, in that the kinetics of hydrogen absorption is accelerated for the as-deposited batch because the activation enthalpy change decreases when more surface defects are present.

3.4 Evolution of crystalline defects with annealing and hydriding

Fig. 12a and Fig.12b show cross-sectional BF-TEM images obtained in as-deposited and annealed Pd films, respectively (see Section 3.1). Fig. 12a reveals the columnar nanograin morphology of the films. It can be seen that several grains are confined within the thickness of the films. The selected-area diffraction pattern (SADP) shown in the lower right part of Fig. 12a reveals that the film exhibits a strong $\langle 111 \rangle$ fcc crystallographic texture. Some growth twins indicated by white arrows can be observed in Fig. 12a. The HRTEM image of Fig. 12c exhib-

its an example of $\Sigma 3 \{111\}$ growth twin boundaries observed in the as-deposited films. Fig. 12b shows that, together with the 525 MPa of tensile stress generated during the annealing cycle, both the morphological texture and the crystallographic texture have been conserved after annealing. However, a clear increase of grain size and aspect ratio of the grains accompanied with a decrease of the number of growth twins can be qualitatively seen in Fig. 12b. Statistical analysis of grain size and TB density has been performed using BF-TEM and DF-TEM in as-deposited, annealed and/or hydrided Pd films. Table 1 summarizes the result of such analysis. First of all, it is clear that both the height and the width of the grains are affected by the grain growth induced by annealing. The average height of the grains increased by a factor 1.6, while their width was more affected, increasing by a factor 1.9. The fraction of grain boundaries was then significantly increased, in the plane of the film as well as in the direction perpendicular to this plane. Although the diffusion of H in Pd is expected to be slowed down by grain boundaries at low concentrations [5], it has to be noted that diffusion is not rate-limiting here - as explained in Section 3.3 - and that the presence of a higher grain boundary density in the as-deposited films actually improves the hydriding kinetics. Additionally, the grain boundaries offer low-energy sites for hydrogen, contributing to the increased H-concentration observed here in the α phase of the Pd-H system [2]. Fig. 12d shows the evolution of dislocation density measured using HRTEM in as-deposited, annealed and/or hydrided Pd films. The scatter in these measurements is caused by the local nature, i.e., individual nanocrystalline grains, used for the HRTEM based measures. In Fig. 12d, the dislocation density is seen to have been decreased by 27% after annealing, then also accelerating the hydriding kinetics [14,15] and increasing the equilibrium H-concentration [1,9]. The twin boundary density has been decreased by 41% (see table 1), which also contributes to the acceleration of the hydriding kinetics [26]. It is worth mentioning here that growth twin boundaries were observed to be connected to grain boundaries. Thus, the decrease of the TB density after annealing is probably due to the shrinking and the disappearance of grains containing

twins. However, although the fact that grain boundaries and lattice dislocations generate saturable, irreversible hydrogen traps is confirmed in this study, twins are unlikely to generate such traps in Pd, as discussed above. Finally, one can notice that, except for the slight increase of dislocation density shown in Fig. 12d, hydrogen cycling in the α phase does not significantly modify the defect concentrations (see table 1 and Fig. 12d).

Conclusions

In this study, the use of an original high resolution in-situ experimental setup allowed adjusting the annealing conditions of Pd thin films in order to obtain specimens with similar internal stresses and different microstructures. It also enabled the study of the hydriding equilibrium and kinetics at room temperature for the as-deposited and annealed specimens. The analysis of the internal stress level at equilibrium and after pumping down brought the following conclusions: the concentration of reversible traps in the palladium lattice is not significantly affected by annealing, while the concentration of saturable, irreversible traps is decreased. The use of a self-consistent kinetic model allowed to identify the rate-limiting steps involved in the hydriding mechanism. An important effect of microstructure on both the adsorption and absorption kinetics has been observed. The quantitative kinetic analysis confirmed these tendencies, by showing an effect on both rate constants for dissociative adsorption and surface-to-bulk transition. In particular, it has been shown that the absorption kinetics of the as-deposited specimens is accelerated as a result of a destabilisation of the thin film surface which is on the order of 10% of the energy of the regular surface sites. A complementary TEM analysis revealed a combined effect of annealing on the densities of grain boundaries, dislocations and twins, supporting our results obtained on both hydriding kinetics and thermodynamics.

Acknowledgements

This work was funded by the Belgian National Science Foundation through a FRIA doctoral fellowship. The authors also acknowledge the support of the Belgian Interuniversity Attraction Poles (IAP) programme (7/21).

References

- [1] Pundt A, Kirchheim R. *Annu Rev Mater Res* 2006;36:555.
- [2] Weissmüller J, Lemier C. *Phys Rev Lett* 1999;82:213.
- [3] Mütschele T, Kirchheim R. *Scripta Metall* 1987;21:135.
- [4] Mütschele T, Kirchheim R. *Scripta Metall* 1987;21,1101.
- [5] Yao J, Cahoon J. *Acta Metall Mater* 1991;39,119.
- [6] Janssen S, Natter H, Hempelmann R, Striffler T, Stuhr U, Wipf H, Hahn H, Cook JC. *Nano Mater* 1997;9:579.
- [7] Kirchheim R. *Prog Mater Sci* 1988;32:261.
- [8] Oudriss A, Creus J, Bouhattate J, Savall C, Peraudeau B, Feaugas X. *Scripta Mater* 2012;66:37.
- [9] Myers SM, Baskes MI, Birnbaum HK, Corbett JW, DeLeo GG, Estreicher SK, Haller EE, Jena P, Johnson NM, Kirchheim R, Pearton SJ, Stavola MJ. *Rev Mod Phys* 1992;64:559.
- [10] Pivak Y, Schreuders H, Slaman M, Griessen R, Dam B. *Int J Hydrogen Energy* 2011;36:4056.
- [11] Maxelon M, Pundt A, Pyckhout-Hintzen W, Barker J, Kirchheim R. *Acta Mater* 2001;49:2625.
- [12] Maxelon M, Pundt A, Pyckhout-Hintzen W, Kirchheim R. *Scripta Mater* 2001;44:817.
- [13] Kirchheim R. *Acta Metall* 1981;29:835.
- [14] Tien J, Thompson A, Bernstein I, Richards R. *Metall Mater Trans A* 1976;7:821.
- [15] Mommer N, Hirscher M, Cuevas F, Kronmüller H. *J Alloys Compd* 1998;266:255.
- [16] Fukai Y. *J Alloys Compd* 2003;356-357:263.
- [17] Fukai Y, Ōkuma N. *Phys Rev Lett* 1994;73:1640.
- [18] Isaeva LE, Bazhanov DI, Isaev EI, Eremeev SV, Kulkova SE, Abrikosov IA. *Int J Hydrogen Energy* 2011;36:1254.

- [19] He JH, Dechiaro LF, Knies DL, Hubler GK, Grabowski KS, Moser AE, Dominguez DD, Kidwell DA, Hagelstein PL. *Int J Hydrogen Energy* 2012;37:12351.
- [20] Carr NZ, McLellan RB. *Acta Mater* 2004;52:3273.
- [21] Singh S, Eijt SWH. *Phys Rev B* 2008;78:224110.
- [22] Borgschulte A, Bielmann M, Züttel A, Barkhordarian G, Dornheim M, Bormann R. *Appl Surf Sci* 2008;254:2377.
- [23] Mine Y, Tachibana K, Horita Z. *Mater Sci Eng A* 2011;528:8100.
- [24] Koyama M, Akiyama E, Sawaguchi T, Raabe D, Tsuzaki K. *Scripta Mater* 2012;66:459.
- [25] So KH, Kim JS, Chun YS, Park KT, Lee YK, Lee CS. *ISIJ Int* 2009;49:1952.
- [26] Danaie M, Tao S, Kalisvaart P, Mitlin D. *Acta Mater* 2010;58:3162.
- [27] Amin-Ahmadi B, Idrissi H, Delmelle R, Pardoën T, Proost J, Schryvers D. *Appl Phys Lett* 2013;102:071911.
- [28] Delmelle R, Michotte S, Sinnaeve M, Proost, J. *Acta Mater* 2013;61:2320.
- [29] Wicke E, Brodowsky H. Hydrogen in palladium and palladium alloys, in: Alefeld G, Voelkl J, editors. *Hydrogen in metals*, vol. 2. Berlin: Springer Verlag; 1978.
- [30] Lewis FA. *The palladium hydrogen system*. London: Academic Press; 1967.
- [31] Zhao Z, Sevryugina Y, Carpenter MA, Welch D, Xia H. *Anal Chem* 2004;76:6321.
- [32] Kulprathipanja A, Alptekin GO, Falconer JL, Way JD. *J Membr Sci* 2005;254:49.
- [33] Jewell JJ, Davis BH. *Appl Catal A* 2006;310:1.
- [34] Daniel R, Holec D, Bartosik M, Keckes J, Mitterer C. *Acta Mater* 2011;59:6631.
- [35] Kumar D, Gupta A. *J Magn Magn Mater* 2007;308:318.
- [36] Köstenbauer H, Fontalvo GA, Kapp M, Keckes J, Mitterer C. *Surf Coat Technol* 2007;201:4777.
- [37] Karlsson L, Hörling A, Johansson M, Hultman L, Ramanath G. *Acta Mater* 2002;50:5103.
- [38] Daniel R, Martinschitz K, Keckes J, Mitterer C. *Acta Mater* 2010;58:2621.

- [39] Xu H, Heinrich H, Wiezorek JM, *Intermetallics* 2003;11:963.
- [40] Miller DC, Herrmann CF, Maier HJ, George SM, Stoldt CR, Gall K, *Scripta Mater* 2005;52:873.
- [41] Delmelle R, Bamba G, Proost J. *Int J Hydrogen Energy* 2010;35:9888.
- [42] Proost J, Spaepen F. *J Appl Phys* 2002;91:204.
- [43] Van Overmeere Q, Vanhumbecq JF, Proost J. *Rev Sci Instrum* 2010;81:045106.
- [44] Delmelle R, Proost J. *Phys Chem Chem Phys* 2011;13:11412.
- [45] Smithells CJ. *Metals Reference Book*. 8th ed. London: Butterworths; 2004.
- [46] Thornton JA, *J Vac Sci Technol* 1974;11:666.
- [47] Thornton JA, Tabock J, Hoffman DW. *Thin Solid Films* 1979;64:111.
- [48] Floro JA, Hearne SJ, Hunter JA, Kotula P, Chason E, Seel SC, Thompson CV. *J Appl Phys* 2001;89:4886.
- [49] Ichinohe T, Masaki S, Uchida K, Nozaki S, Morisaki H. *Thin Solid Films* 2004;466:27.
- [50] Smits FM. *Bell Sys Tech J* 1958;37:711.
- [51] Wedler G, Alshorachi G. *Thin Solid Films* 1980;74:1.
- [52] Vries JD. *Thin Solid Films* 1988;167:25.
- [53] Tripodi P, Armanet N, Asarisi V, Avveduto A, Marmigi A, Vinko JD, Biberian JP. *Phys Lett A* 2009;373:3101.
- [54] Shivaprasad SM, Angadi MA. *J Phys D: Appl Phys* 1980;13:L171.
- [55] Hanabusa T, Kusaka K, Sakata O. *Thin Solid Films* 2004;459:245.
- [56] Tada H, Kumpel AE, Lathrop RE, Slanina JB, Nieva P, Zavracki P, Niaoulis IN, Wong PY. *J Appl Phys* 2000;87:4189.
- [57] Kuru Y, Wohlschlägel M, Welzel U, Mittemeijer E. *Surf Coat Technol* 2008;202:2306.
- [58] Colla MS, Wang B, Idrissi H, Schyvers D, Raskin JP, Pardoën T, *Acta Mater* 2012;60:1795.
- [59] Youngdahl CJ, Sanders PG, Eastman JA, Weertman JR. *Scripta Mater* 1997;37:809.

- [60] Peisl H. Lattice strains due to hydrogen in metals, in: Alefeld G, Voelkl J, editors. Hydrogen in metals, vol. 1. Berlin: Springer Verlag; 1978.
- [61] Bucur RV. J Mater Sci 1987;22:3402.
- [62] Krom A, Bakker A. Metall Mater Trans B 2000;31:1475.
- [63] Young GA, Scully J. Acta Mater 1998;46:6337.
- [64] Cao Y, Li H, Szpunar J, Shmayda W. Mater Sci Eng A 2004;379:173.
- [65] Frappart S, Feugas X, Creus J, Thebault F, Delattre L, Marchebois H. J Phys Chem Sol 2010;71:1467.
- [66] Frappart S, Feugas X, Creus J, Thebault F, Delattre L, Marchebois H. J Phys Chem Sol 2012;534:384.
- [67] Froment GG, Bischoff KB, DeWilde J. Chemical reactor analysis and design. 3rd ed. Hoboken, NJ: Wiley; 2010.
- [68] Ward TL, Dao T. J Membr Sci 1999;153:211.
- [69] Legrand E, Bouhattate J, Feugas X, Garmestani H. Int J Hydrogen Energy 2012;37:13574.
- [70] Gesari S, Pronsato M, Juan A. Int J Hydrogen Energy 2009;34:3511.
- [71] Johansson M, Skúlason E, Nielsen G, Murphy S, Nielsen RM, Chorkendorff I. Surf Sci 2010;604:718.

Figure captions

- Fig. 1. Schematic representation of the original setup used in this study. The red lines represent the trajectory of the laser beams. A top view of the CCD screen is also provided, showing the reflected laser spots.
- Fig. 2. Evolution of the stress*thickness product as a function of time (before and during Ti layer deposition, as well as after Pd deposition) and Pd thickness (during Pd deposition) using 2 different argon sputtering pressures.
- Fig. 3. Evolution of the ratio $\Delta R/R_0$ as a function of temperature during a heating cycle performed in the range 20 - 350°C with a heating rate of 25°C and a 5 min temperature plateau.
- Fig. 4. TCR of Pd thin films with different thicknesses, fitted with Eq. (5). The value for bulk Pd is also shown (taken from Ref. [51]).
- Fig. 5. Evolution of the internal stress in a Pd thin film as a function of temperature, measured during the first 5000 sec of the annealing cycle, including the heating phase, the temperature plateau and part of the cooling phase. The last point is the mean of a 500 sec measurement performed at room temperature.
- Fig. 6. Evolution of the internal stress as a function of time during two hydriding cycles recorded, respectively, using an as-deposited Pd thin film and a film annealed 20 min at 300°C.

- Fig. 7. Equilibrium absolute stress as a function of $p_{H_2}^{1/2}$ in the α phase region of the Pd-H system. Two batches with similar internal stresses are compared, one being subjected to hydrogen cycling as-deposited and the other one after annealing 20 min at 300°C.
- Fig. 8. Slope of the first linear kinetic regime as a function of p_{H_2} , fitted with Eq. (11) and including the linear p_{H_2} -dependence of k'_{ab} (see Ref. [28]).
- Fig. 9. Slope of the second linear kinetic regime as a function of p_{H_2} , fitted with Eq. (10).
- Fig. 10. Rate constant for hydrogen absorption as a function of p_{H_2} . Linear fits are shown for each set of specimens.
- Fig. 11. Schematic energy level diagram for H-adsorption/absorption into Pd, showing the effect of microstructure on the activation enthalpy for hydrogen absorption.
- Fig. 12. BF micrographs of cross-sectional FIB foils of (a) as deposited Pd films and (b) after annealing at 300 °C for 20 min. Growth twins are indicated by white arrows. Corresponding selected area diffraction patterns are presented in each figure. (c) HRTEM image of growth twin boundaries in the as-deposited films. (d) Average dislocation density (red solid squares) evolution in the Pd films. Numbers beside unfilled circles indicate the corresponding grain size (nm) of individual measures.

Table 1. Argon plasma pressure p_{Ar} , thickness t_f , average growth-induced stress σ_0 and TEM defect statistics of the Pd films studied in this work: grain height (perpendicular to the plane of the film) and width (in the plane of the film), aspect ratio (minimum and maximum values) and TB density. Data is provided for as-deposited specimens, as well as after annealing and hydriding (α -phase, $p_{H_2} = 11$ mbar).

p_{Ar} [Pa]	t_f [nm]	σ_0 [MPa]	Specimen state	Grain height [nm]	Grain width [nm]	Aspect ratio [-]	TB den- sity [$1/\mu\text{m}^3$]
0.92	157	491	As-dep.	81 ± 6	31 ± 3	1 - 4	9300 ± 600
			After H_2	86 ± 7	30 ± 3	1 - 4	9460 ± 600
			-35 As-dep.	102 ± 13	42 ± 6	1 - 4	8600 ± 500
0.46	156	490	After anneal.	160 ± 5	79 ± 5	1 - 2	5066 ± 300
			After anneal. + H_2	162 ± 6	82 ± 5	1 - 2	5200 ± 400

Figure 1

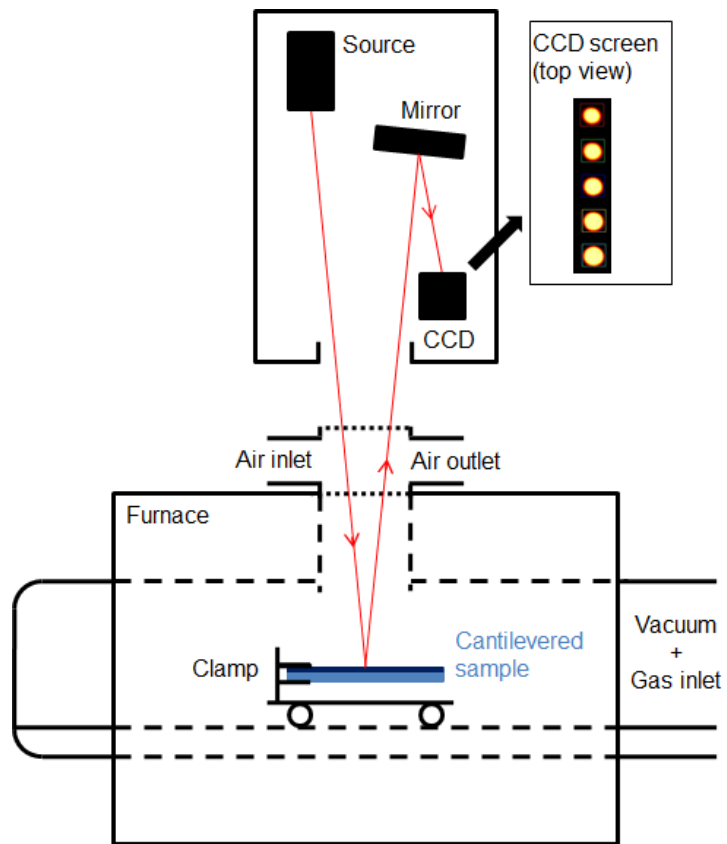


Figure 2

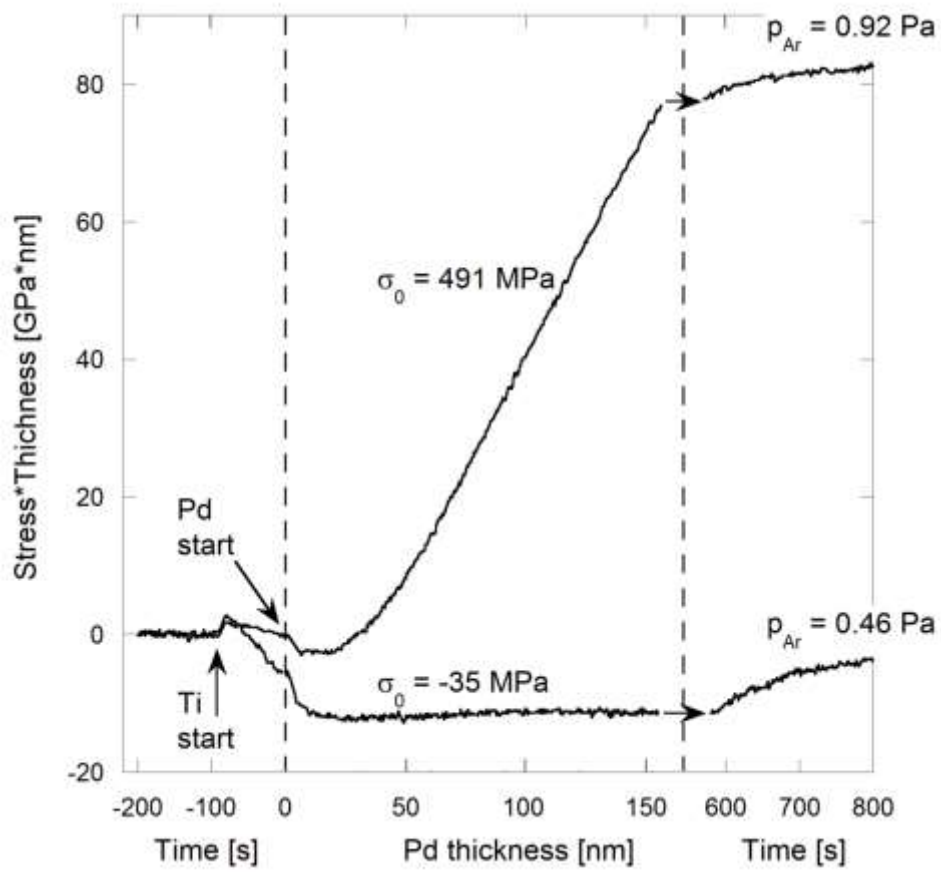


Figure 3

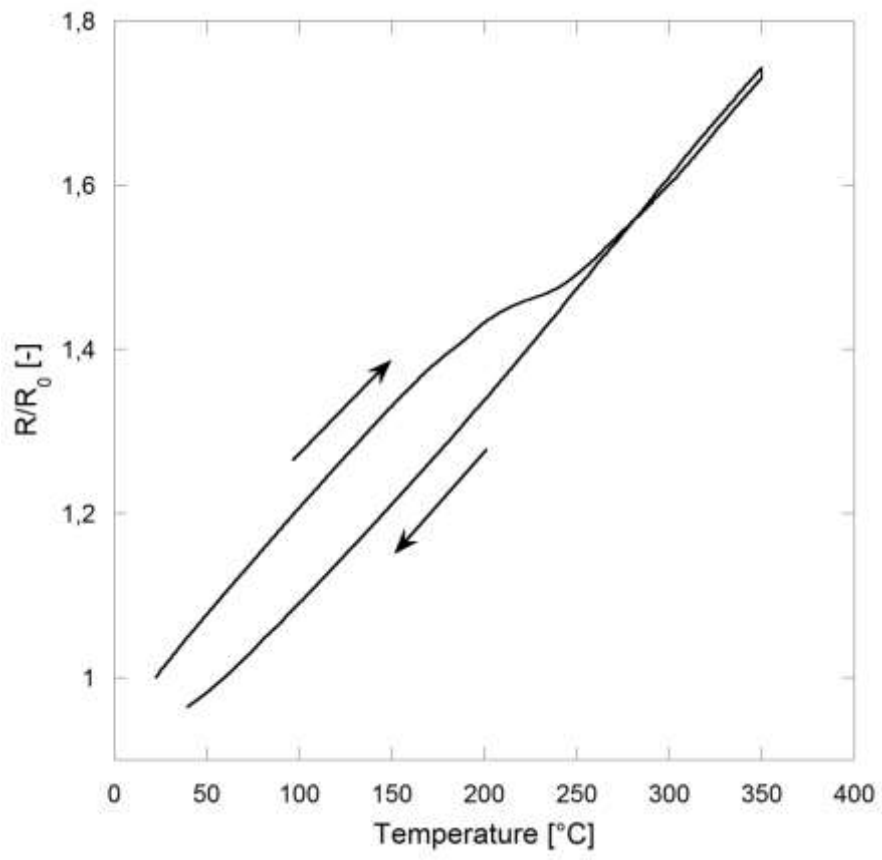


Figure 4

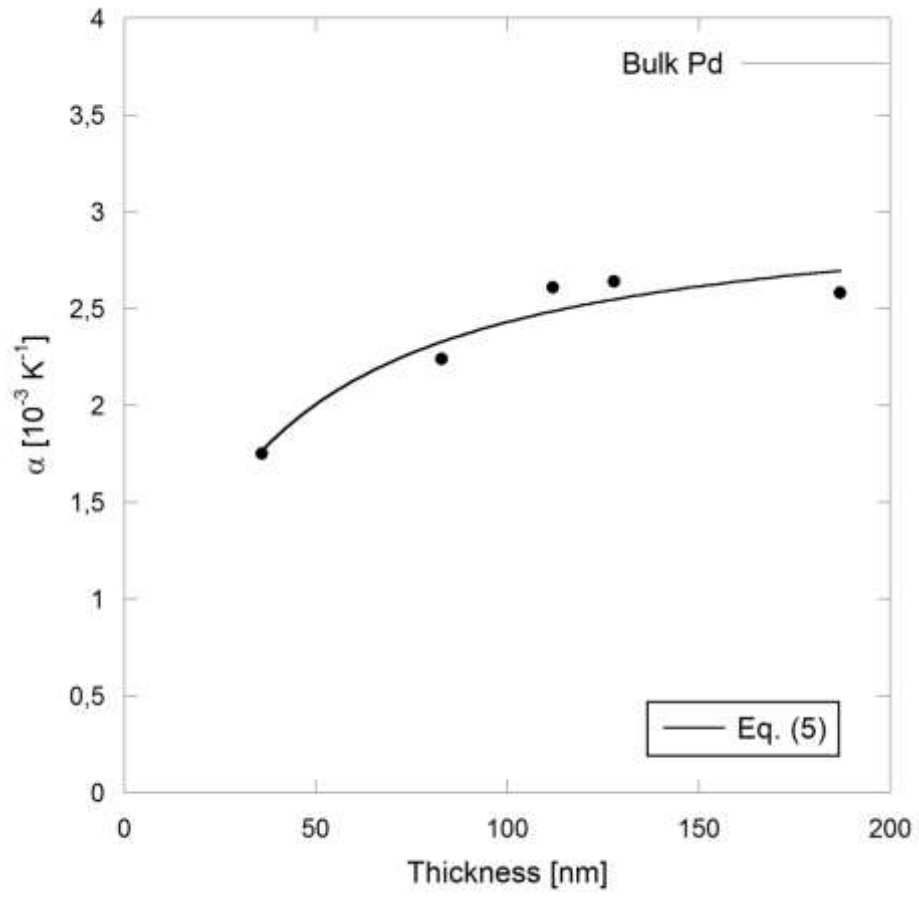


Figure 5

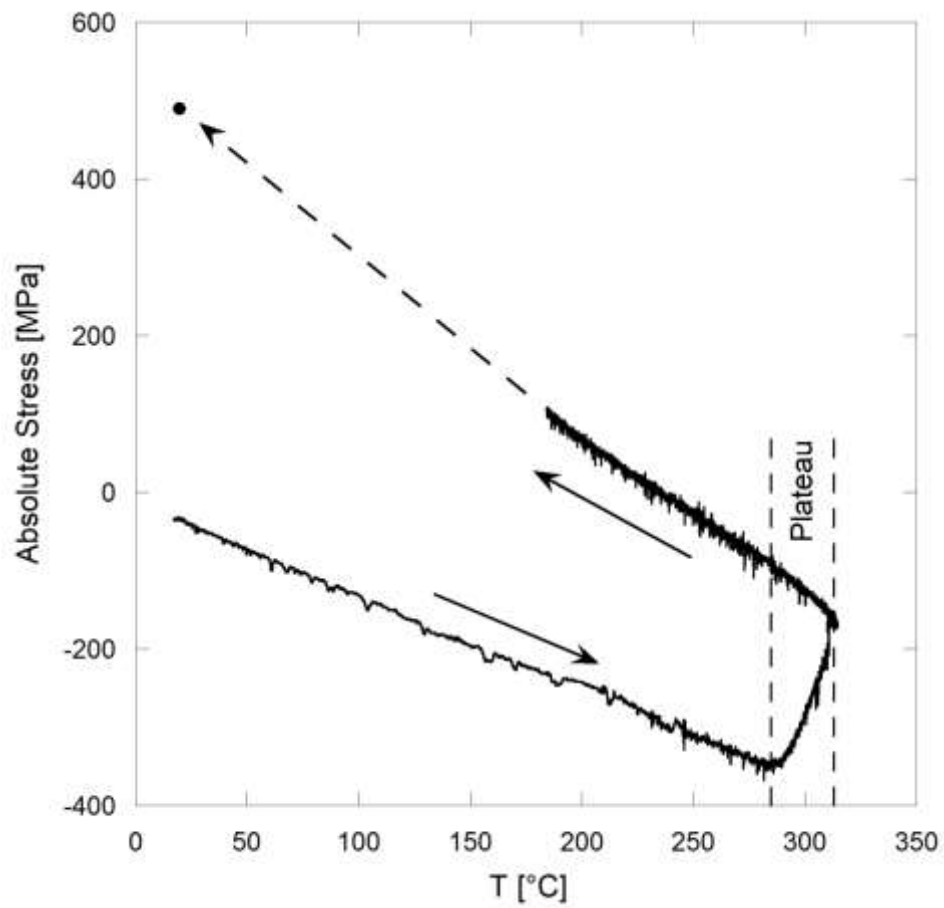


Figure 6

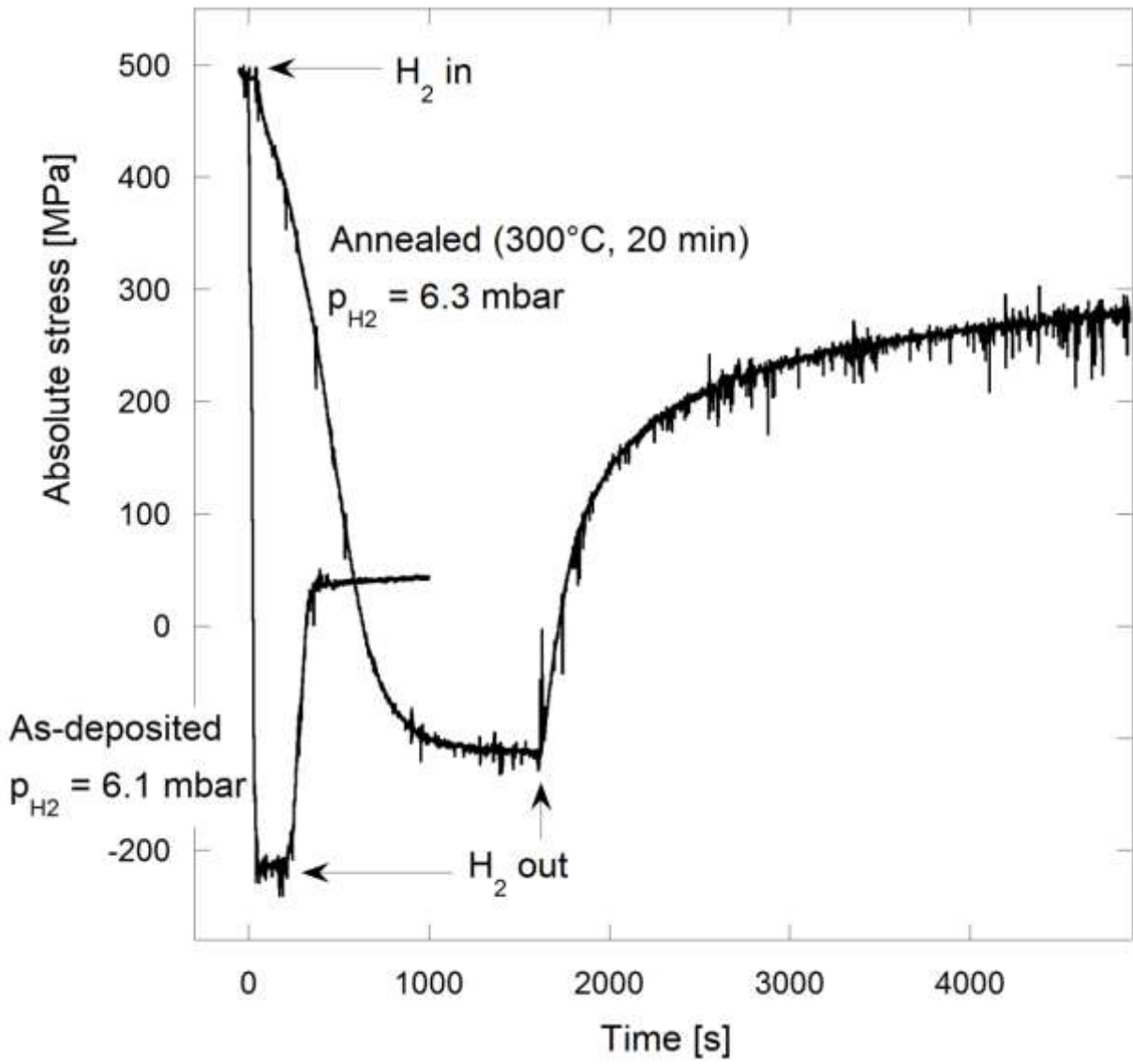


Figure 7

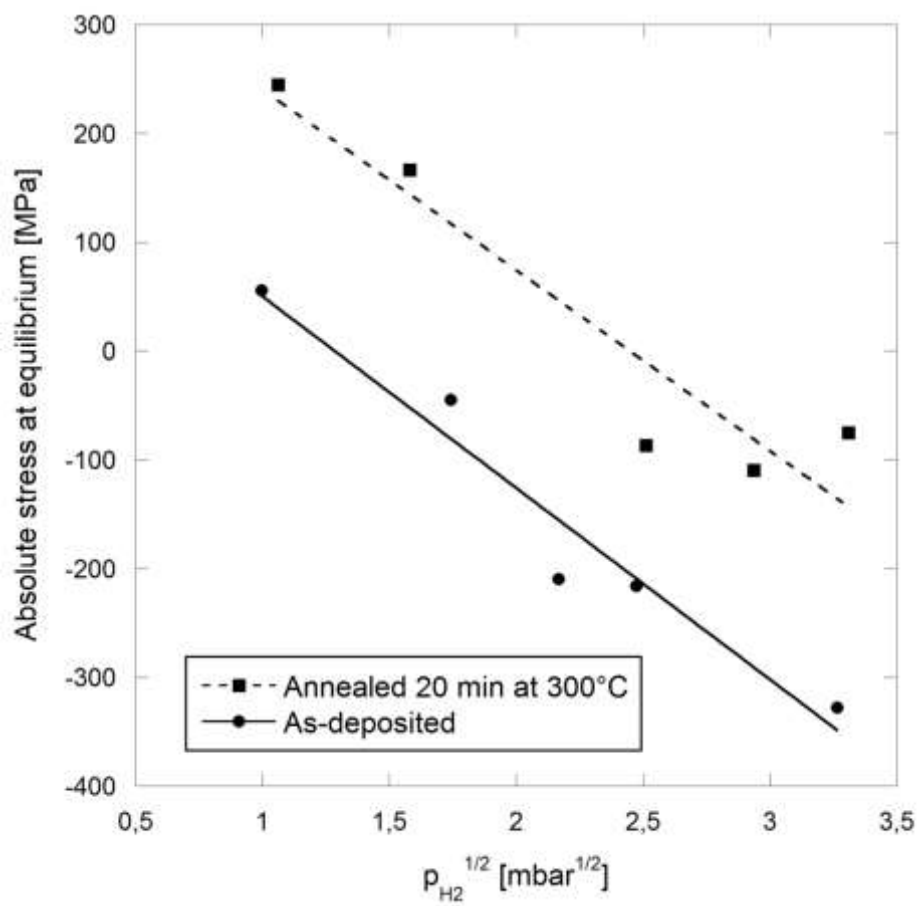


Figure 8

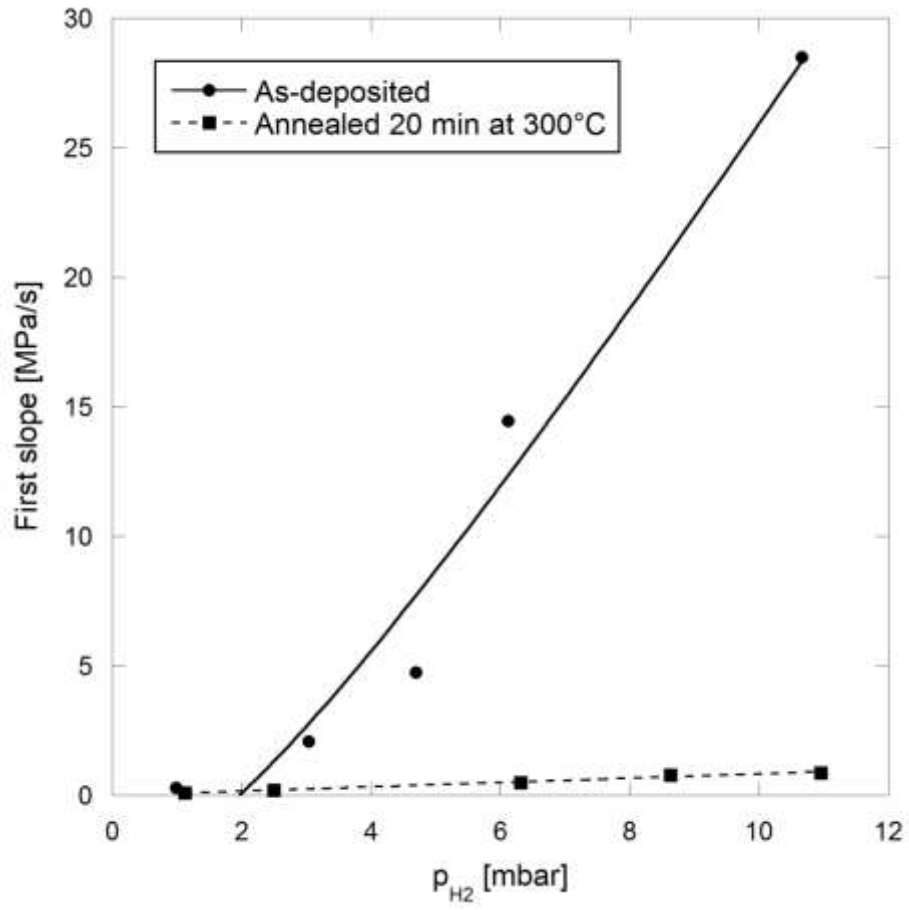


Figure 9

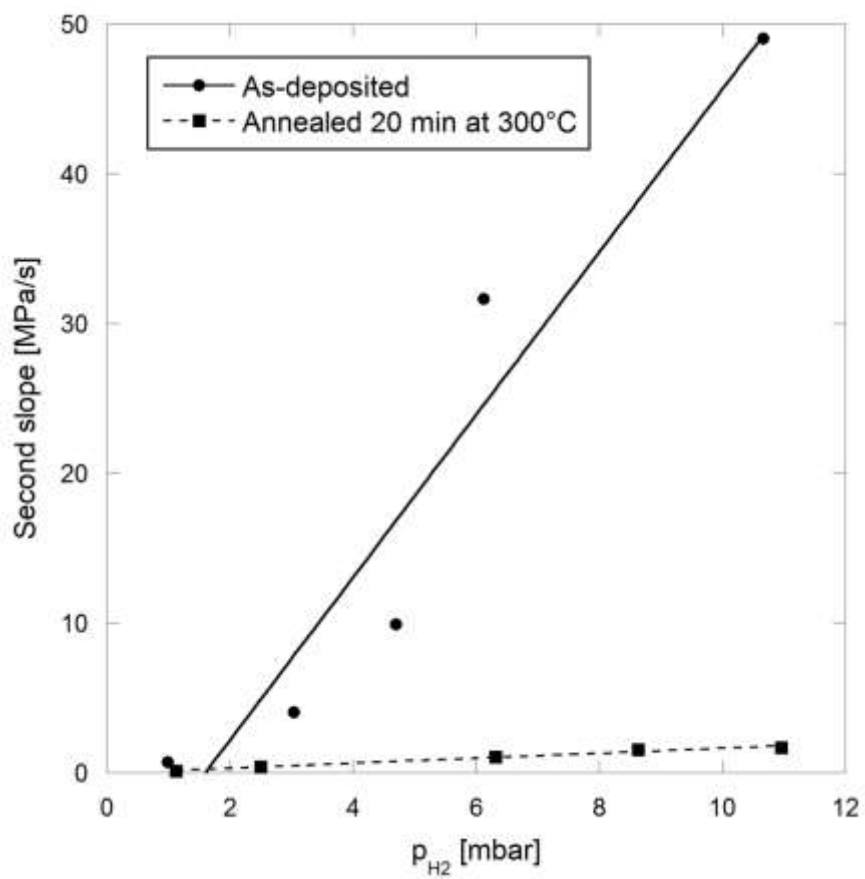


Figure 10

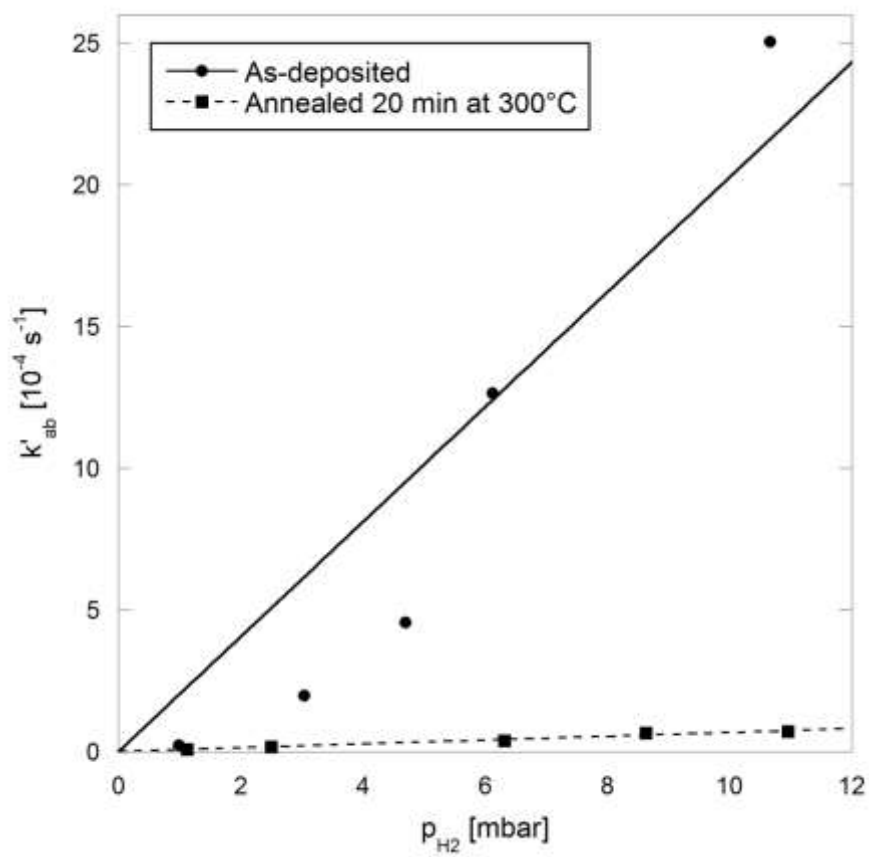
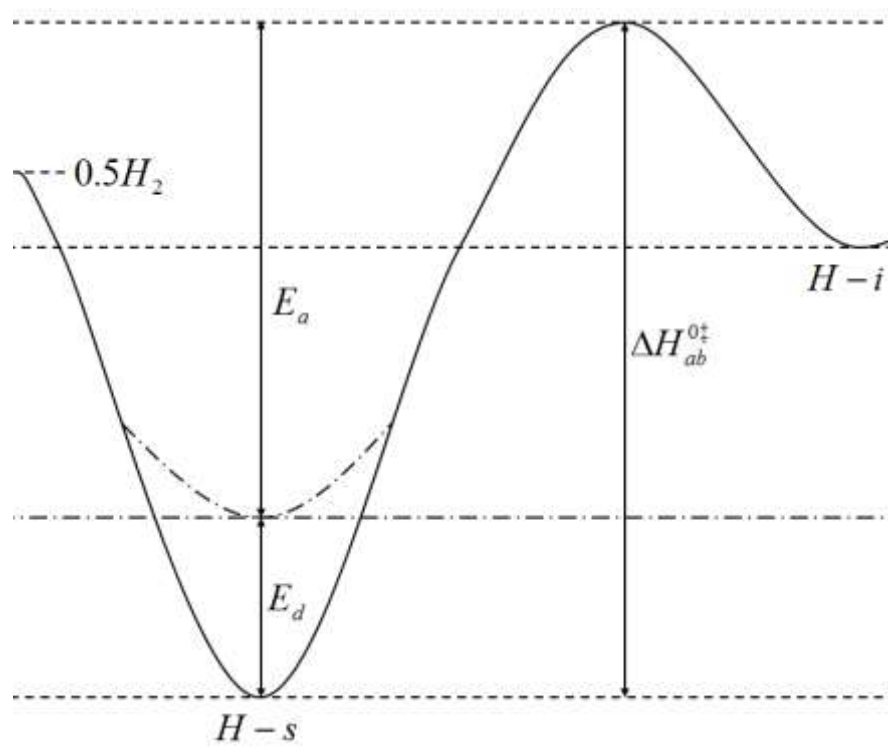


Figure 11



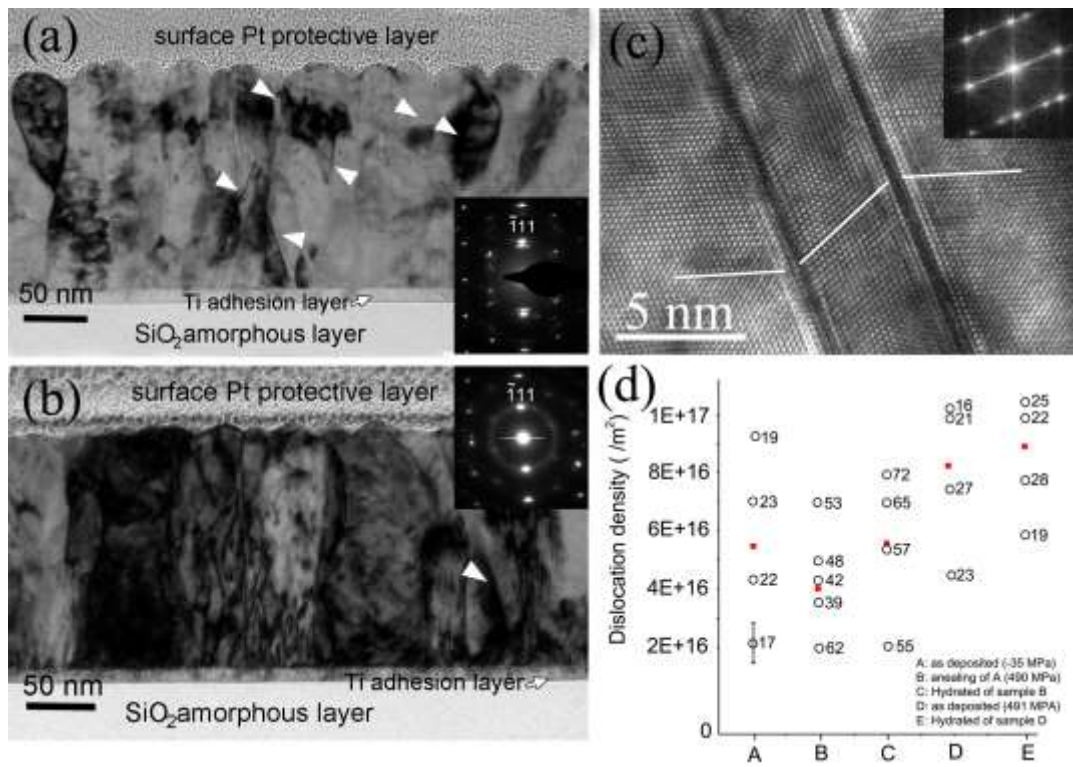


Figure 12